Systematic theoretical study of carbon nanotubes rolled from a two-dimensional tetrahex-carbon nanosheet

Guang Yang [1,2,*] Ying Yang [2,3] and Xihong Peng [2,†]

[1]*School of Science, Hebei University of Science and Technology, Shijiazhuang 050018, People's Republic of China*
[2]*College of Integrative Sciences and Arts, Arizona State University, Mesa, Arizona 85212, USA*
[3]*School of Automation and Information Engineering, Xi'an University of Technology, Xi'an, Shaanxi 710048, People's Republic of China*

A recently proposed two-dimensional (2D) carbon allotrope, tetrahex-carbon composed of tetragonal and hexagonal rings in a buckled plane, draws scientific research interests due to its remarkable mechanical and electronic properties, including ultrahigh strength, negative Poisson's ratio, finite direct band gap, and high carrier mobility. In this work, a series of carbon nanotubes rolled from this new 2D tetrahex-C nanosheet with various size and chirality are studied through first-principles density-functional theory calculations. The tube diameter is in the range of 4.5–18 Å. It is found that the smallest thermodynamically stable nanotubes have the diameter of 4.5 Å for zigzag tetrahex-C nanotubes (z-TH-CNTs) and 6.0 Å for armchair tetrahex-C nanotubes (a-TH-CNTs). The z-TH-CNTs are energetically more favorable than the a-TH-CNTs given similar size. The single-wall nanotubes have a particular wall thickness which shrinks with the decrease of tube size. It is also found that all explored nanotubes show semiconducting behavior and HSE predicted band gaps can be effectively tuned in the range of 1.84–2.69 eV with size and chirality. Large curvature in small z-TH-CNTs alters the band structures, resulting in a significantly reduced effective mass of electron thus indicating potentially enhanced carrier mobility. Work function of the tubes can be manipulated within the range of 5.25–5.43 eV dependent on the tube size and chirality. These remarkable structural and electronic properties in the tetrahex-C nanotubes may have potential applications in nanoelectronics.

I. INTRODUCTION

Carbon is capable of forming many allotropes, including three-dimensional (3D) diamond and graphite, two-dimensional (2D) graphene [1–3], one-dimensional (1D) carbon nanotubes (CNTs) [4–9], and zero-dimensional (0D) fullerenes [10]. Intensive studies have revealed that low-dimensional carbon nanomaterials exhibit remarkable properties, which are critical for scientific research and have promising potential applications in future electronics. In addition to 2D graphene, enormous other 2D allotropes of carbon were proposed, such as S graphene [11], T graphene [12], various phases of carbon sheets [13,14], and α, β, and δ graphynes [15,16]. Recently, a 2D carbon allotrope called tetrahex carbon was theoretically proposed and derived from penta-graphene [17] using Stone-Wales transformation [18] by Ram and Mizuseki [19]. Tetrahex C, composed of tetragonal and hexagonal of carbon rings in a buckled plane, is energetically more favorable than penta-graphene and presents a direct band gap with high electron mobility $\sim 10^4 \, \text{cm}^2/(\text{V s})$ [19]. More interestingly, it was found that this material exhibits excellent mechanical properties such as ultrahigh ideal strength outperforming both graphene and penta-graphene and intrinsic in-plane negative Poisson's ratio [20]. In addition, it

demonstrates high anisotropy in carrier mobility which can be effectively tuned by the application of uniaxial strain [21]. These remarkable properties in tetrahex C imply potential applications in nanomechanics and nanoelectronics.

1D CNTs [4–9,22] can be generated by rolling 2D monolayer of graphene and penta-graphene. It is well known that the graphene nanotubes demonstrate either metallic or semiconducting properties [4–9] with the variation of tube sizes although graphene has zero band gap. It was also found that the penta-graphene nanotubes present semiconducting properties and the band gap can be manipulated by the tube sizes and strain [22] which open up potential applications for optoelectronic devices. These special properties of nanotubes are distinct from those in their corresponding 2D counterparts and are attractive in practical applications of electronics. In this study, we are interested in the CNTs created from the 2D tetrahex-C nanosheet. We systematically investigated the tetrahex-C nanotubes (TH CNTs) with various tube diameters and chirality. We found that the TH CNTs are thermodynamically stable. Their electronic properties, including band structure, band gap, effective masses of charge carriers and work function, are a strong function of tube size and chirality.

II. COMPUTATIONAL METHODS

The first-principles density-functional theory (DFT) [23] calculations were performed utilizing the Vienna *ab initio* simulation package (VASP) [24,25]. The interactions between

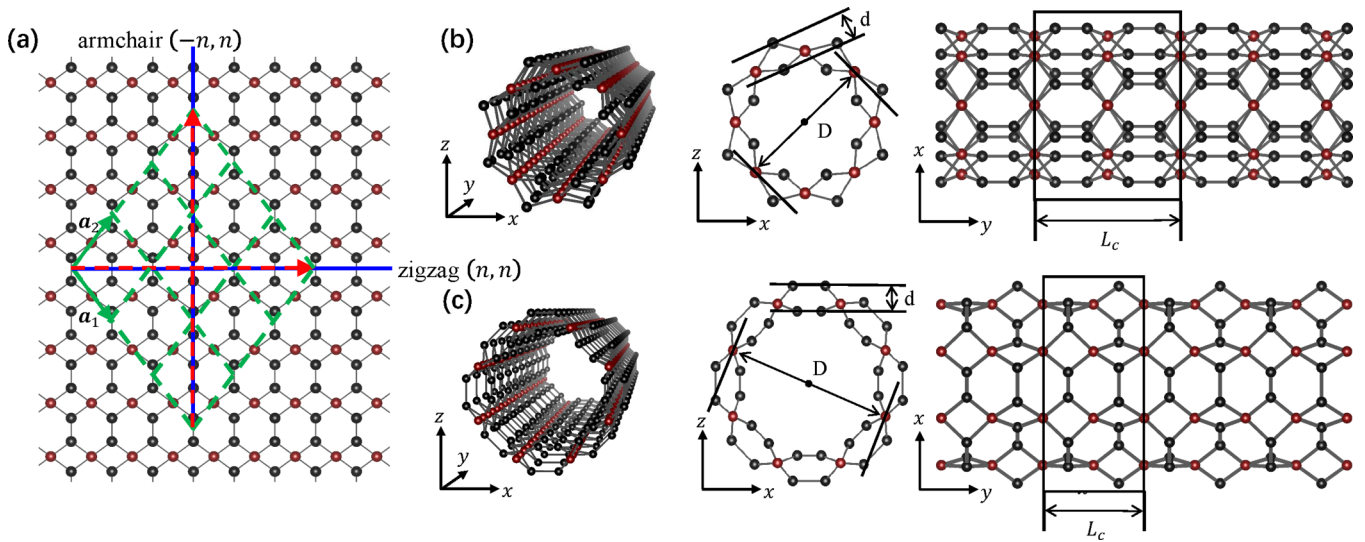*gyangphys@hebust.edu.cn
†xihong.peng@asu.edu

FIG. 1. (a) Top view of the monolayer tetrahex-C nanosheet. The lattice vectors a_1 and a_2 are denoted by the green solid lines with arrows. The minimum dashed diamond in green represents a primitive cell. The sp^2- and sp^3-hybridized carbon atoms are represented by black and brown balls, respectively. z-TH-CNTs and a-TH-CNTs can be produced by rolling up the sheet along the zigzag and armchair directions, respectively. Two red dashed lines containing arrows gives the roll-up vectors of z-TH-CNT (3, 3) and a-TH-CNT (−3, 3), respectively. Snapshots of the tube structures with different views for (b) z-TH-CNT (4, 4) and (c) a-TH-CNT (−4, 4). The nanotube axial direction is along the y axis with a lattice constant L_c. The tube diameter is denoted as D and the wall thickness is labeled as d.

ion cores and valence electrons are treated by the projector-augmented wave (PAW) [26,27] potentials. The Perdew-Burke-Ernzerhof (PBE) exchange-correlation functional [28] was used to carry out general electronic structure calculations and geometry relaxation. Electronic band structures are also calculated through the hybrid Heyd-Scuseria-Ernzerhof (HSE)06 method [29,30], which can predict a high accuracy band gap of semiconductor due to the mixture of Hartree-Fock (HF) exact exchange functional and the PBE functional in its exchange-correlation functional. A vacuum space of 20 Å is added to the system in order to avoid the interactions between the system and its images resulting from periodic boundary conditions. The valence electron wave functions are expanded by the plane-wave basis set with kinetic-energy cutoff of 500 eV. The reciprocal space is meshed using the Monkhorst-Pack method [31] with a grid density of less than $2\pi \times 0.02 \text{ Å}^{-1}$. The energy convergence for electronic iterations during self-consistent calculations is set to be 10^{-5} eV. For ionic iterations during geometry relaxations, the convergence criteria of the total energy and the force are set to be 10^{-4} eV and 10^{-3} eV/Å, respectively. 21 k points are collected along high-symmetry lines in the first Brillouin zone for the band-structure calculations. The supercell method in PHONOPY [32] code is utilized to compute phonon spectrum with atomic forces being calculated in the framework of the density-functional perturbation theory (DFPT). In the DFPT calculations, the plane-wave kinetic-energy cutoff is set to be 900 eV, and the energy for electronic and ionic iterations is converged to 10^{-6} and 10^{-5} eV, respectively.

III. RESULTS AND DISCUSSION

A. Structure and stability

Figure 1(a) presents the top view of the 2D monolayer of tetrahex carbon. Its sandwichlike structure is constructed

by sp^2 and sp^3 hybridized carbon atoms illustrated by black and brown spheres, respectively [19]. Its primitive unit cell contains six atoms shown by the minimum diamond denoted by the green dashed lines, and its lattice vectors are a_1 and a_2 shown by the green solid lines with arrows. From our calculations, the optimized lattice constants of tetrahex carbon are $a_1 = a_2 = 3.80$ Å, buckling thickness $d = 1.16$ Å, and the angle between the lattice vectors $\theta = 106.8°$, which are consistent with literature [19–21].

Nanotubes can be generated by rolling up the tetrahex-carbon monolayer along any vector $\boldsymbol{R} = m\boldsymbol{a}_1 + n\boldsymbol{a}_2$ which defines a pair of integer indexes (m, n) representing various chirality of the TH CNTs. Here, we mainly focus on the zigzag and armchair tetrahex-carbon nanotubes (abbreviated as z-TH-CNTs and a-TH-CNTs) having the indexes (n, n) and $(−n, n)$, respectively. Therefore, the size of the tube can be denoted by the parameter n and in the following text we use n_z and n_a to represent the size of the z-TH-CNTs and a-TH-CNTs, respectively. As an example, in Fig. 1(a), two red dashed lines containing arrows along the zigzag and armchair directions represent the rolling vectors for the (3, 3) z-TH-CNT and (−3, 3) a-TH-CNT, respectively. Figures 1(b) and 1(c) display the snapshots of the zigzag (4, 4) and armchair (−4, 4) tubes. The diameter D of the tube is defined as the distance between two sp^3-hybridized carbon atoms (the brown spheres in Fig. 1) passing through the center of the tube. Since the 2D tetrahex-C nanosheet is in a bucked plane with a buckling thickness, there is a wall thickness of the tube, which is denoted by d as shown in Figs. 1(b) and 1(c). The axial direction of the tube is along the y axis with a lattice constant L_c.

The z-TH-CNTs (n, n) and a-TH-CNTs $(−n, n)$ with a tube diameter in the range of 4.5–18 Å are explored in this work. For the z-TH-CNTs, the tube diameter D is between 4.54 and 17.35 Å with the parameter n_z ranging from 3 to 12. And for the a-TH-CNTs, D is in the range of 6.02–17.55 Å with n_a
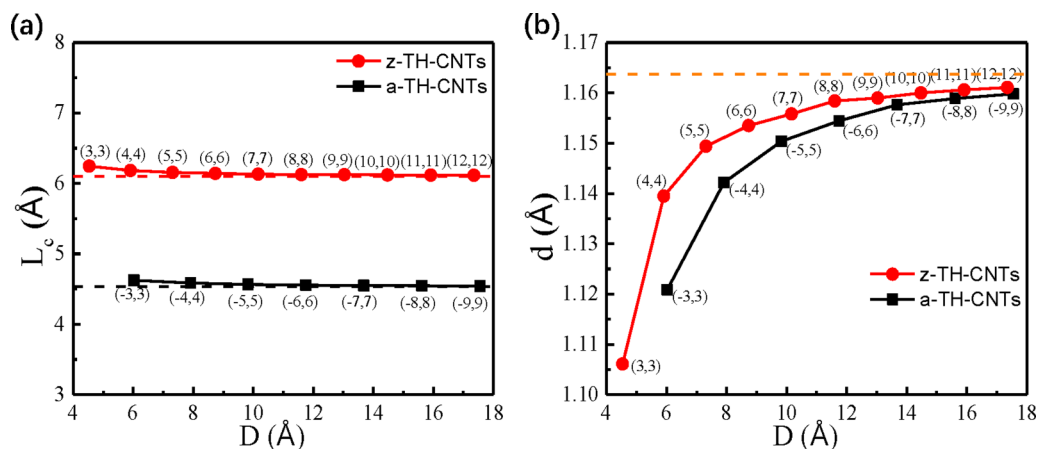
FIG. 2. (a) The lattice constant L_c, and (b) wall thickness d of the nanotubes as a function of the tube diameter D. The dashed lines represent their corresponding values in the 2D monolayer.

between 3 and 9. Figures 2(a) and 2(b) display the relation between the tube diameter and typical lattice parameters of the optimized z-TH-CNTs and a-TH-CNTs. In Fig. 2(a), the red and black dashed lines show the corresponding lattice constant values of L_c (6.11 and 4.53 Å along the armchair and zigzag directions, respectively) in the 2D tetrahex-C nanosheet. It is found that L_c in the tubes has negligible change compared to its 2D values except for a tiny increase for ultrasmall tubes. However, the tube wall thickness d exhibits a dramatic variation with the tube size. The wall thickness d of z-TH-CNTs increases from 1.11 to 1.16 Å for the diameter D ranging from 4.54 to 17.35 Å. On the other hand, the wall thickness d in a-TH-CNTs changes from 1.12 to 1.16 Å for the diameter D in the range of 6.02–17.55 Å. It is clear that the wall thicknesses of tubes with increasing diameter approach the corresponding value (1.16 Å) in 2D tetrahex-C sheet given by the dashed lines in Fig. 2(b). Furthermore, for a similar size of tubes, the wall thickness d shows more shrinkage in the a-TH-CNTs than z-TH-CNTs.

Cohesive and strain energies of the tubes are plotted in Fig. 3 to explore the energetic stability of the TH-CNTs. The cohesive energy is obtained by the formula

$E_c = (E_{total} - N \times E_{atom})/N$, where E_{total} is the total energy of the unit cell, N is the number of the carbon atoms in the cell, and E_{atom} is the energy of an isolated carbon atom. The strain energy E_s is defined as the difference between the energies in the nanotube and in the 2D monolayer of tetrahex C. As shown in Fig. 3(a), the cohesive energy for the 2D tetrahex-C nanosheet is calculated as a reference, presented by the black dashed line. Both cases of nanotubes show that the cohesive energies are approaching that of the 2D tetrahex-C nanosheet with the increasing size of tubes. The cohesive energies of z-TH-CNTs fall between -7.08 and -6.66 eV with the tube diameter D ranging from 4.54 to 17.35 Å. For a-TH-CNTs, these appear in the range of -7.06 and -6.76 eV with D in the region of 6.02–17.55 Å. According to the literature [22], γ and β phases of penta-graphene nanotubes exhibit cohesive energies in the range of -6.90 and -6.55 eV as D in the region of 4.85–13.11 Å and those of the α phase have cohesive energy between -7.15 and -6.65 eV with D in the range of 3.56–13.24 Å. This implies that the z-TH-CNTs and a-TH-CNTs are the metastable phases between them.

For both cases of tetrahex-C nanotubes, the strain energy increases with the reduction of the tube diameter and their
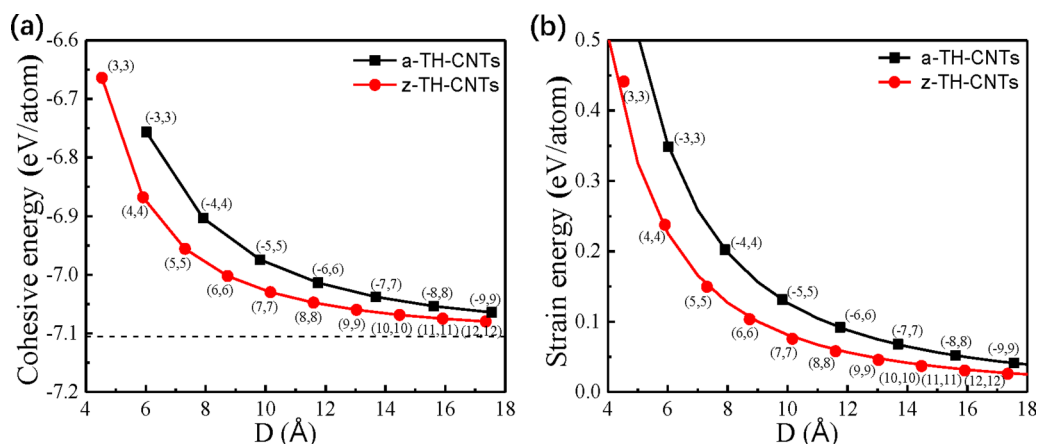

FIG. 3. (a),(b) the cohesive and strain energies of the z-TH-CNTs and a-TH-CNTs as a function of the tube diameter. The dashed line in (a) represents the cohesive energy in the 2D monolayer. The strain energies in (b) are fitted to c/D^2 behavior by the solid lines.
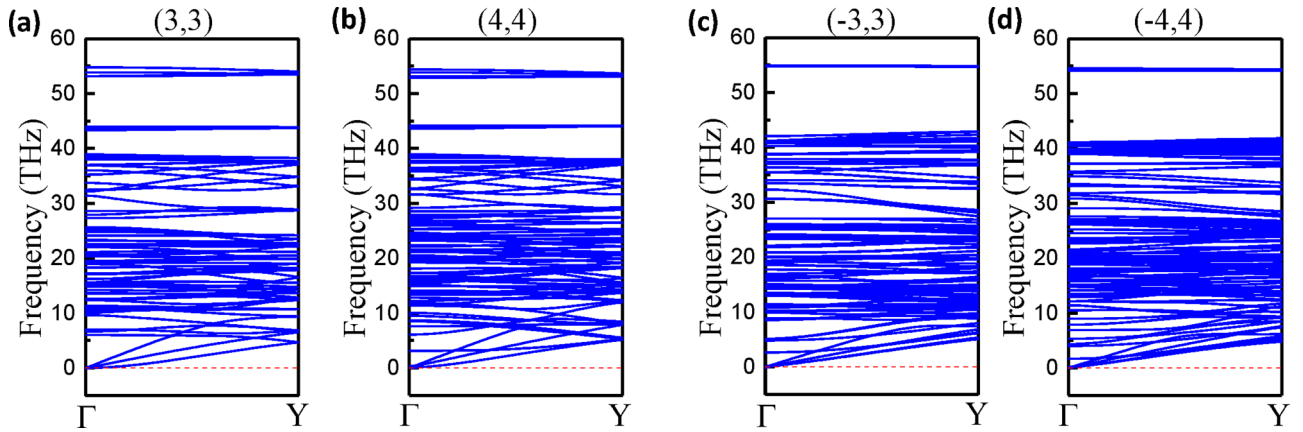
FIG. 4. The phonon spectra for the zigzag (a) (3, 3) and (b) (4, 4), the armchair (c) (−3, 3) and (d) (−4, 4) nanotubes. Absence of negative frequencies indicates thermodynmical stability of these tubes.

function relation is fitted by c/D^2 [the black and red solid lines in Fig. 3(b)]. The fitting parameter c is 8.12 and 12.66 for the z-TH-CNTs and a-TH-CNTs, respectively. From Fig. 3, the cohesive and strain energy of z-TH-CNTs are both smaller than those of the a-TH-CNTs given the same size of tubes, indicating that z-TH-CNTs are energetically more favorable than a-TH-CNTs.

All of the studied nanotubes in this work are proven to be thermodynamically stable through the calculations of their phonon spectra. The thermodynamic stability is confirmed by the absence of imaginary frequencies in the entire Brillouin zone. It is found that the smallest sizes of the stable tubes are (3, 3) for the z-TH-CNTs and (−3, 3) for the a-TH-CNTs. Figure 4 presents the phonon spectra of the zigzag (3, 3) and (4, 4), armchair (−3, 3) and (−4, 4) tubes, as examples.

B. Electronic properties of z-TH-CNTs and a-TH-CNTs

1. Band structure

Figure 5(a) presents the band structure of 2D mono-layer tetrahex C. The valence-band maximum (VBM) and conduction-band minimum (CBM) are both located at the Γ point suggesting a direct band gap. The gap value is 1.62 eV

based on the PBE functional and 2.65 eV from HSE functional, which are in great agreement with literature [19–21]. The inset of Fig. 5(a) shows the first Brillouin zone in a shape of hexagon with k_1 and k_2 representing the basis vectors in the reciprocal space of 2D tetrahex-C nanosheet.

From the tetrahex-C sheet, we can roughly estimate the band structures of the nanotubes using a simple zone-folding method without considering the effect of tube curvature [33–35]. In addition to the roll-up vector $\boldsymbol{R} = m\,\boldsymbol{a}_1 + n\,\boldsymbol{a}_2$ for the nanotubes, a translation vector is defined as $\boldsymbol{T} = p\,\boldsymbol{a}_1 + q\,\boldsymbol{a}_2$, where there is no common divisor between p and q in order to specify the unit cell. $\boldsymbol{R}$ and $\boldsymbol{T}$ construct a rectangular supercell which specifies the unrolled unit cell for the nanotubes. The roll-up direction has a finite size and the translation vector is along the tube axis and repeated period-ically. The translational invariance yields the first Brillouin zone along the tube axis determined by $\boldsymbol{k}_\parallel$, which satisfies the equation $\boldsymbol{T}\boldsymbol{k}_\parallel = 2\pi$. Specifically, $\boldsymbol{k}_\parallel = \frac{1}{2}(-k_1 + k_2)$ and $\boldsymbol{k}_\parallel = \frac{1}{2}(k_1 + k_2)$ along the tube axis for z-TH-CNTs and a-TH-CNTs, respectively. And the corresponding first Brillouin zones along the tube axis span in the range of $-\frac{1}{2}\boldsymbol{k}_\parallel$ to $+\frac{1}{2}\boldsymbol{k}_\parallel$. In addition, rolling up the nanosheet into a tube intro-duces a periodic boundary condition along the circumferential
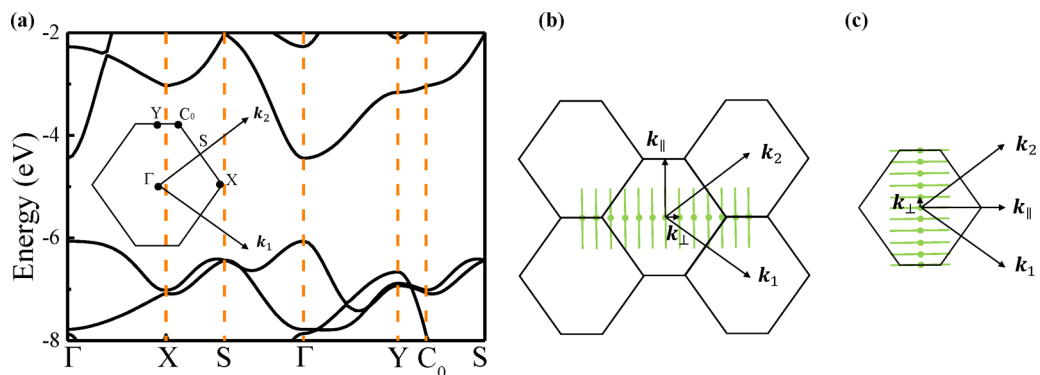

FIG. 5. (a) The PBE predicted band structure of the 2D tetrahex-C nanosheet. The inset of (a) presents the first Brillouin zone with high symmetric points, namely Γ, X, S, C_0, and Y. The basis vectors in the reciprocal space are denoted by $\boldsymbol{k}_1$ and $\boldsymbol{k}_2$. The energy is referenced to vacuum. The projection of the reciprocal vectors of (b) z-TH-CNT (6, 6) and (c) a-TH-CNT (−5, 5). $\boldsymbol{k}_\parallel$ and $\boldsymbol{k}_\perp$ represent the translational and roll-up vectors in the reciprocal space, respectively.
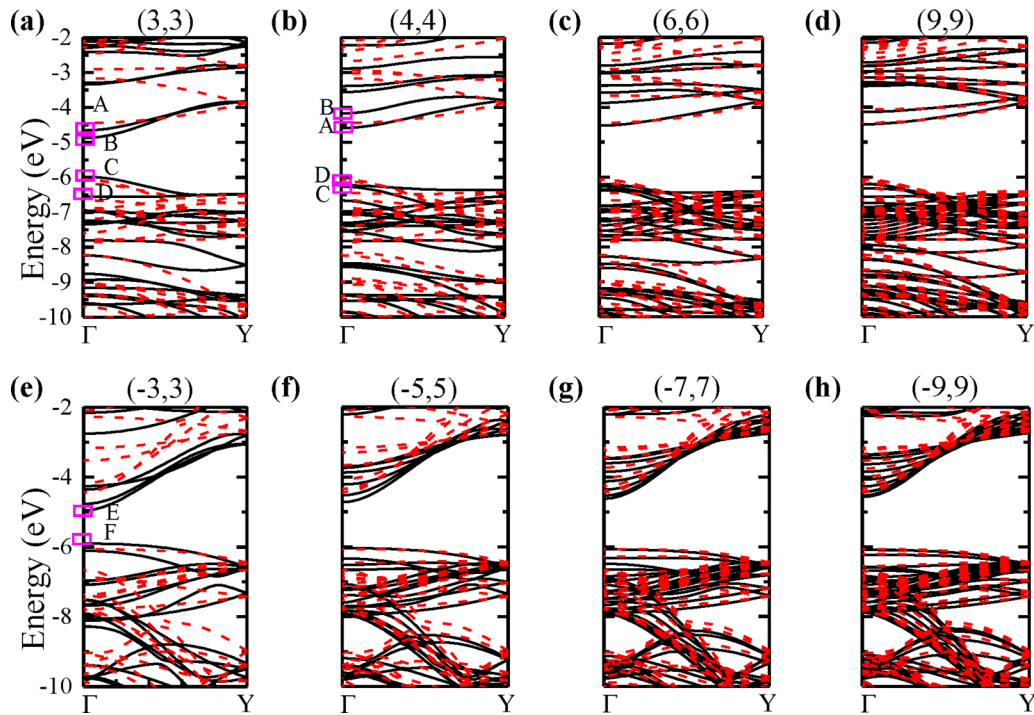
FIG. 6. The PBE predicted band structure (solid black lines) of z-TH-CNTs (top) and a-TH-CNTs (bottom), compared to the zone folding approach (red dashed lines). The tube chirality is labeled on the top of each figure. The energy is referenced to the vacuum level. The near-edge states are labeled as A–F. States B and C represents the CBM and VBM, respectively in the tube (3, 3). States E and F correspond the CBM and VBM, respectively in the tube (−3, 3). State A (D) is at the band right above (below) the CBM (VBM) in the tube (3, 3). The corresponding states A–D for the tube (4, 4) are also shown in (b).

direction (i.e., the direction of the roll-up vector $\boldsymbol{R}$) in the nanotube. It means that the wave function ψ of the unrolled nanosheet satisfies the Bloch theorem as $\psi(\boldsymbol{r} + \boldsymbol{R}) = e^{i k_\perp \boldsymbol{R}} \psi(\boldsymbol{r}) = \psi(\boldsymbol{r})$. Here, another reciprocal vector $k_\perp$ needs to be introduced and has to satisfy the equation of $\boldsymbol{R} k_\perp = 2\pi l$ (l is integer). Thus, $\boldsymbol{k}_\perp = \frac{l}{2n_z}(k_1 + k_2)$ for z-TH-CNTs and $\boldsymbol{k}_\perp = -\frac{l}{2n_a}(k_1 - k_2)$ for a-TH-CNTs. Their corresponding shortest reciprocal vectors in 2D tetrahex-C nanosheet are $\boldsymbol{k}_\perp = k_1 + k_2$ and $\boldsymbol{k}_\perp = -(k_1 - k_2)$ for z-TH-CNTs and a-TH-CNTs, respectively. It determines that the number of the different modes along the roll-up vector are $2n_z$ ($l = -n_z + 1, -n_z + 2, \ldots, n_z - 1, n_z$) and $2n_a$ ($l = -n_a + 1, -n_a + 2, \ldots, n_a - 1, n_a$) for z-TH-CNTs and a-TH-CNTs, respectively. It readily obtains the projection of the nanotube reciprocal vectors on the Brillouin zone of the tetrahex-C sheet by using $k_\parallel$ and $k_\perp$. Figures 5(b) and 5(c) give examples of reciprocal vector projection in the (6, 6) z-TH-CNT and (−5, 5) a-TH-CNT, respectively. Based on these relations, the band structures of the nanotubes can be roughly estimated by folding the band structures of the tetrahex-C sheet. The band structures of the nanotubes from such a zone folding method are given by the red dashed lines in Fig. 6, which does not yet include the curvature effect of the tubes.

The advanced *ab initio* DFT method is needed to predict the actual band structures of the nanotubes including the effect of curvature. Figure 6 shows the DFT obtained band structure, compared to that obtained using the zone-folding method. It is found that both z-TH-CNTs and a-TH-CNTs are semiconductors with a direct band gap.

For both z-TH-CNTs and a-TH-CNTs, the discrepancy between solid (with curvature effect) and dashed (without curvature effect) lines is negligible in the larger nanotubes, for instance, (9, 9) and (−9, 9) in Figs. 6(d) and 6(h), respectively. This is resulted from the fact that larger tubes have smaller curvature and their structures are relatively close to the monolayer of tetrahex C when compared to smaller tubes. On the other hand, in smaller tubes, the significant effect of curvature gives rise to the remarkably modified band structures. For example, for the tubes (3, 3) and (−3, 3) in Figs. 6(a) and 6(e), respectively, the conduction bands near the Γ point are prominently lower than their zone-folding ones, while the valence bands have a slight increase of the energy.

In order to understand in detail the curvature effect on the band structure in the small tubes, we analyzed various states near the Fermi level which is defined as the middle of the gap. It is found that for the z-TH-CNTs, CBM is a singly degenerate state while VBM is a doubly degenerate state. However, for the a-TH-CNTs, both CBM and VBM are singly degenerate.

As an example, Fig. 7 displays the electron density contour plots of several states A–D (labeled in Fig. 6) for the tubes (3, 3) and (4, 4) and their corresponding *spd*-orbital projections. The inner and outer sp^2 C dimers in the tubes are represented by the numbers 1 and 3. The middle sp^3 carbons are denoted by the number 2. Due to the curvature effect, the charge distribution and hybridization pattern of the states near the Fermi level vary with the tube size, as shown in Fig. 7. For both tube cases, state A (singly degenerate) has an
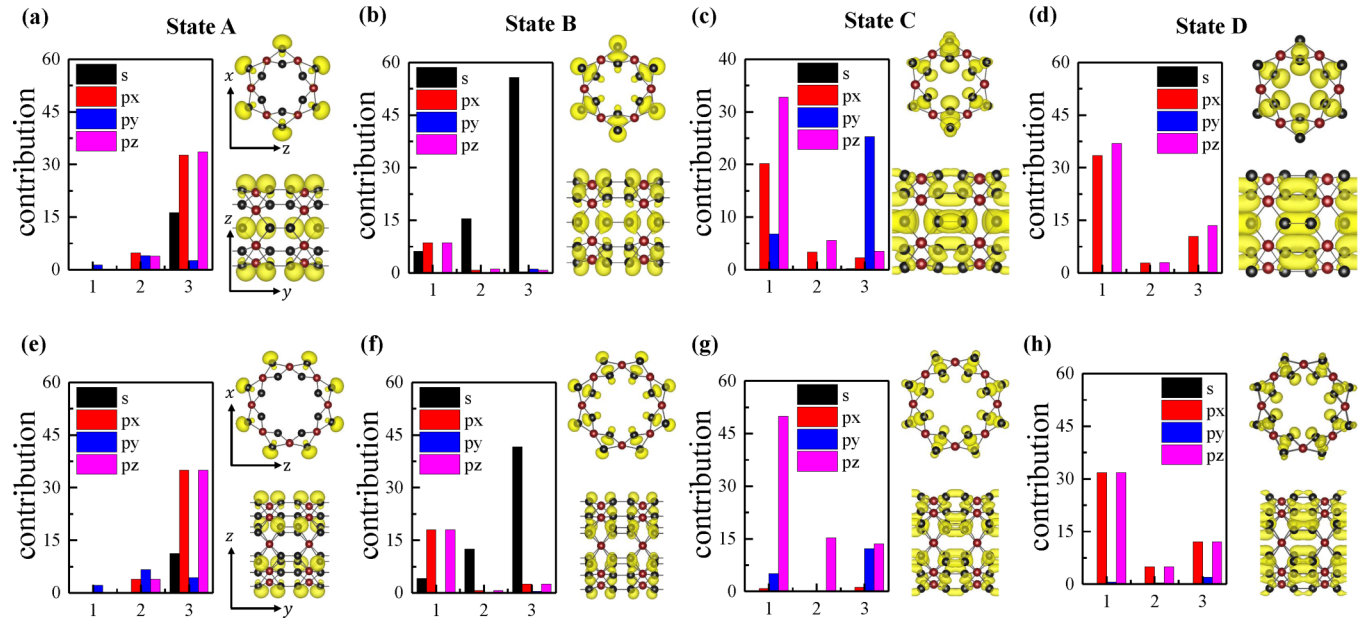
FIG. 7. The *spd*-orbital projection (the left of each subfigure) and electron density contour (the right of each subfigure) plots of near-edge states (a)–(d) A–D for the tube (3, 3) and (e),(f) A-D for the tube (4, 4). The electron density contour plots with the views along the tube axis (i.e., the *y* axis) (up) and the *x* axis (down) for each state are shown. For the plots of the *spd*-orbital projection, the inner and outer sp^2 carbon dimers are represented by the numbers 1 and 3. The middle sp^3 carbon atom is labeled as 2.

antibonding character and is contributed by a mixed s, p_x, and p_z orbitals with the electron cloud mainly distributed on the outer sp^2 carbon dimers. State B (single degenerate) also has an antibonding pattern and is dominantly contributed by the s orbitals on the outer sp^2 carbon dimers. It is revealed that the proportion of the s orbitals increases with the decrease of the tube size. State D (doubly degenerate) has a bonding nature and is predominantly contributed by the p_x and p_z orbitals on the inner carbon dimers. Although state C for both tube chiralities is doubly degenerate, the plot of its *spd*-orbital projection is distinct. For the tube (3, 3), state C is mainly contributed by a mixed p_y orbital on the outer sp^2 carbon dimers and p_x, p_z orbitals on the inner sp^2 carbon dimers, which exhibits a bonding characteristic. However, state C in the tube (4, 4) is dominated by the p_z orbital only on the inner sp^2 carbon dimers.

Interestingly, Comparing Figs. 6(a) and 6(b), it is found that the energy of state A is lower than that of state B in the tube (4, 4). Therefore, state A represents the CBM of the tube. Meanwhile, the energy of state C drops lower than state D in the tube (4, 4) and becomes the VBM. These energy crossovers cause the distinction of the band structure near the Fermi level.

On the other hand, for the a-TH-CNT (−3, 3) and (−5, 5), Fig. 8 presents the electron cloud distributions in states E and F (i.e., the CBM and VBM, respectively), and their *spd*-orbital compositions, respectively. It was found that both states E and F are singly degenerate. State E has an antibonding nature with electron density mainly contributed by the p_x and p_z orbitals, while state F has a bonding characteristic. From Fig. 8, both states for the tubes (−3, 3) and (−5, 5) show that the charge density located at the outer sp^2 carbon dimers is significantly larger than that on the middle sp^3 and inner sp^2 carbon atoms.

According to the above discussion, the charge density of states near the Fermi level for z-TH-CNTs and a-TH-CNTs is predominantly located at the outer and inner sp^2 carbon dimers. Therefore, it is important to examine the bond length of those carbon dimers as a function of the tube size, in order to better understand the energy variation of these near-Fermi states. The results are presented in Fig. 9. α_o and α_i represent the bond lengths of the outer and inner sp^2 carbon dimers, respectively. It is clear from Fig. 9 that these bond lengths of the C dimers vary with the tube diameter and experience an intrinsic strain. According to the definition of strain, $\varepsilon = \frac{\alpha - \alpha_0}{\alpha_0}$, where α_0 is the bond length of the sp^2 carbon dimer in the 2D tetrahex-C nanosheet, the outer C dimers are stretched and experience an intrinsic tensile strain as shown in Fig. 9(a). More specifically, for z-TH-CNTs with n_z larger than 4 and all a-TH-CNTs studied in this work, the bond length of the outer C dimer α_o increases with the reduction of tube diameter D, suggesting an enhanced tensile strain in the small tubes. In detail, the intrinsic tensile strain in the outer dimer for z-TH-CNTs increases from 0.69% to 1.30% as n_z drops from 12 to 4 and that for a-TH-CNTs increases from 1.34% to 3.78% as n_a reduces from 9 to 3. However, in Fig. 9(a), the intrinsic tensile strain in the smallest z-TH-CNT (3, 3) has a sharp drop to a value of 0.84% comapred to that 1.30% in the tube (4, 4). This may result from the significant structural reconstruction in this smallest tube (3, 3) since it has the largest axial lattice constant and thinnest wall thickness as suggested in Fig. 2.

The bond length α_i of the inner C dimers as shown in Fig. 9(b) is smaller than that in the 2D monolayer, indicateing an instrinsic compressive strain. The value of α_i generally decreases with the reduciton of the tube diameter, suggesting a larger compressive strain in the inner C dimers for small tubes. In detail, the compressive strain increases from 0.72%
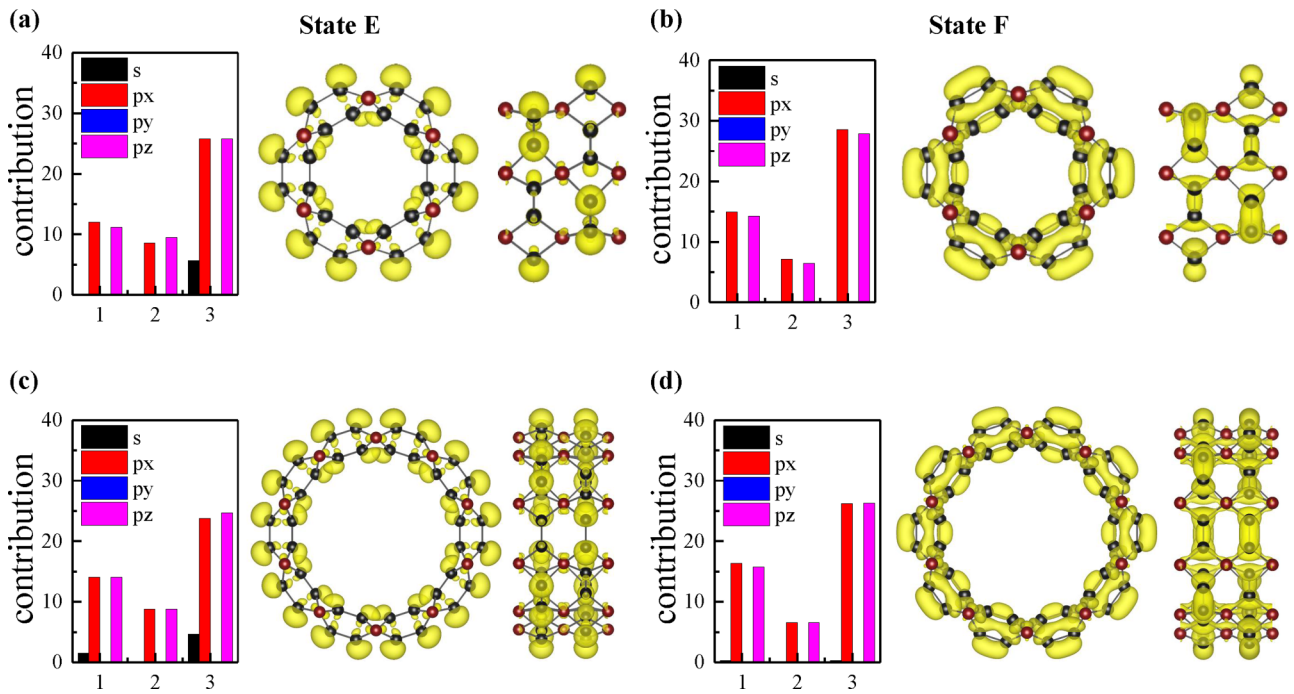
FIG. 8. The *spd*-orbital projection and electron density contour plots of near-edge states (a),(b) E and F for the tube $(-3, 3)$ and (c),(d) E and F for the tube $(-5, 5)$. The electron density contour plots with the views along the tube axis (i.e., the y axis) (middle) and the x axis (right) for each state are shown. For the plots of the *spd*-orbital projections, the inner and outer sp^2 carbon dimers are represented by the numbers 1 and 3. The middle sp^3 carbon is labeled 2.

to 1.72% as n_z in z-TH-CNTs reduces from 12 to 4 and the strain increases from 1.16% to 2.41% with n_a in a-TH-CNTs drops from 9 to 3. Examing data in Fig. 9, it is also found that α_o has a larger value for a-TH-CNTs than that for z-TH-CNTs given a similar tube size, while α_i is smaller for a-TH-CNTs compared to that for z-TH-CNTs. Therefore, the corresponding intrinsic strain in the outer/inner C dimers in a-TH-CNTs is larger than that in z-TH-CNTs. This is consistent with the results in Fig. 3 that the cohesive and strain energies in a-TH-CNTs are larger than that in z-TH-CNTs for a given tube size.

From literature [20,36,37], compressive strain generally increases the energy of an antibonding state while it decreases

that of a bonding state. In contrast, tensile strain in general reduces the energy of an antibonding state while it lifts that of a bonding state. These are well consistent with the behaviors observed in our TH-CNTs. For example, in z-TH-CNTs with n_z greater than 4, the CBM is an antibonding state (i.e., state A) and its charge is dominantly spreading at the outer sp^2 carbon dimers. As discussed above, the outer C dimers experience an intrinsic tensile strain, thus lowers the energy of the CBM with the reduction of tube diameter, which is in great agreement with the results in Fig. 6. On the other hand, the VBM of z-TH-CNTs is a bonding state (i.e., state C) when n_z is greater than 5. Its charge density is primarily distributed on the inner carbon dimers. The inner C dimer
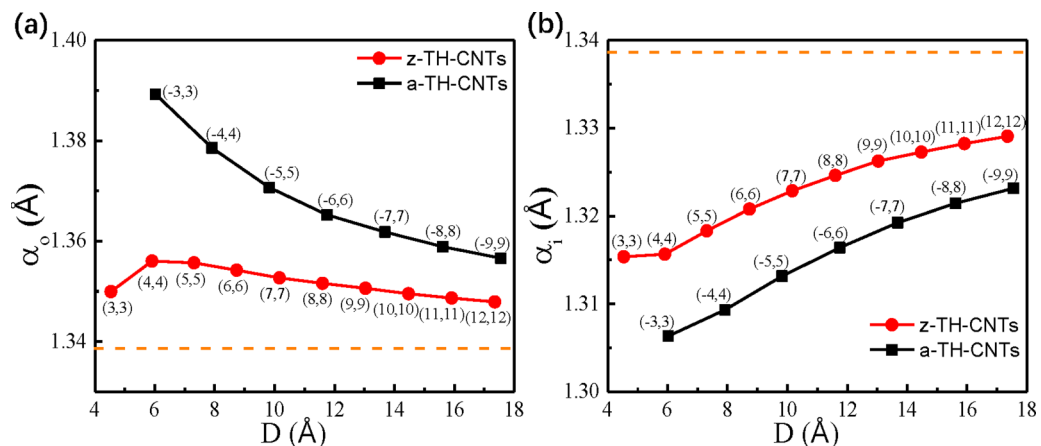

FIG. 9. The bond length (denoted by α_o and α_i) of the (a) outer and (a) inner sp^2 carbon dimers for z-TH-CNTs and a-TH-CNTs as a function of tube size, respectively. The dashed lines refer to the bond length of the sp^2 carbon dimer in the 2D monolayer of tetrahex C.
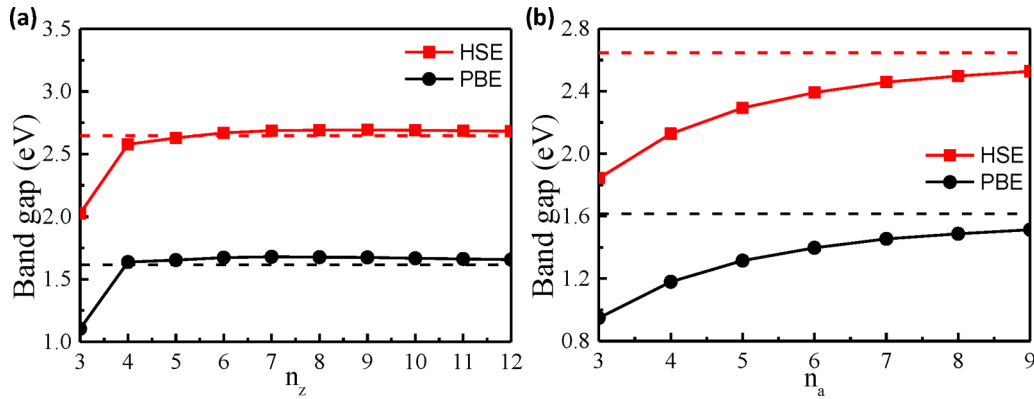
FIG. 10. The band gaps of (a) z-TH-CNTs and (b) a-TH-CNTs as a function of tube size using PBE and HSE functionals, respectively. The dashed lines refer to the band gap in the2D monolayer tetrahex C.

withholds an intrinsic compressive strain which is expected to reduce the energy of the VBM with the decrease of the tube size. Compared to state C, state D has a smaller difference of the charge density distribution between the outer and inner dimers. Therefore, the energy of state C decreases more sharply than that of state D for the tube (4, 4), which is consistent with the results in Figs. 6(b)–6(d). However, for the tube (3, 3), the proportion of a strong bonding p_z orbital located at the outer dimers surges up and the intrinsic tensile strain pushes up the energy of state C to represent the VBM as shown in Fig. 6(a). In summary, for z-TH-CNTs with tube size n_z larger than 4, the intrinsic strain in the outer/inner C dimers lowers the energies of the VBM and CBM which leads to the decrease of the Fermi level. And for the smallest tube (3, 3), the significant reduction of the energy of state B further decreases the Fermi level.

On the other hand in the a-TH-CNTs, the energy variations of the CBM and VBM are smoother compared to that in z-TH-CNTs. The antibonding state E and bonding state F both have larger charge density distributed on the outer carbon dimer. The intrinsic tensile strain in the outer C dimer reduces the energy of the antibonding state E (i.e., CBM) and increases that of the bonding state F (i.e., VBM), resulting in a smaller band gap in the narrow tubes as shown in Fig. 6. Due to the larger difference of the charge density between outer and inner dimers for state E, its energy shifts due to strain is much more evident than that of state F, which also leads to a lower Fermi level in the narrow tubes.

2. Band gap

As seen from the band structure of the nanotubes, the band gap is a strong function of the tube size and chirality as shown in Fig. 10. It is well known that standard DFT including PBE functional underestimates band gaps of semiconductors. The advanced HSE hybrid method has a better prediction of the gaps. In Fig. 10, we present the band gap predicted by the PBE and HSE methods in which both functionals illustrate a consistent trend for the band-gap variation with tube size. Due to the strain effect on reducing the energies of the CBM and VBM with a similar extent for the tubes (4, 4) to (12, 12), the band gap of the z-TH-CNT ranging from 1.64 to 1.66 eV (2.58 to 2.68 eV) for PBE (HSE) is close to that of the 2D

tetrahex-C sheet, which is denoted by the red dashed lines for HSE and black dashed lines for PBE in Fig. 10(a). However, there is a sharp drop of the band gap for the tube (3, 3) to 1.10 eV (2.03 eV) for PBE (HSE) due to the energy crossover between states A and B, C and D near the gap under the influence of hybridization and intrinsic strain aforementioned. Distinctively in Fig. 10(b), the band gap of the a-TH-CNT increases from 0.95 to 1.51 eV (1.84 to 2.53 eV) for PBE (HSE) approaching that of the 2D tetrahex-C sheet as the size of the tube increases. This trend of band gap for the a-TH-CNT mainly results from the significant decrease of energy of CBM in the band structure of smaller tubes, which is derived from intrinsic strain and charge distribution effect, as is discussed previously.

3. Effective mass

The carrier effective mass is defined as $m^* = \hbar^2 (\frac{\partial^2 E}{\partial k^2})^{-1}$, where $\hbar$ is the reduced Plank constant, E refers to the energy of conduction band for electron or valence band for hole, and k represents the reciprocal wave vector. The effective masses of electron and hole for various sizes of nanotubes are calculated using a five-point second derivative with the k-point spacing smaller than $0.015 \,\text{Å}^{-1}$ to eliminate nonparabolic effects. The results are presented in Fig. 11. As the diameter of the z-TH-CNT increases, the effective mass of the electron shows an approximately linear increase from $0.31 m_e$, to $1.10 m_e$, which is smaller than that in 2D tetrahex-C sheet ($1.77 m_e$) along the armchair direction [19,21]. This complies with the decreasing curvature of the conduction band around the CBM (originated from the intrinsic strain) as the increase of the tube's size shown in Figs. 6(a)–6(d). The effective mass of the hole displays a sharp decrease from $1.33 m_e$, to $0.38 m_e$ approaching that in 2D tetrahex-C sheet ($0.34 m_e$) [19,21] when n_z increases from 4 to 12. However, for $n_z = 3$, the effective mass of the hole drops sharply to $0.44 m_e$ in Fig. 11(a). These effects are forecasted in Figs. 6(a)–6(d). From Figs. 6(b)–6(d), the less flattening of the valence band in the vicinity of the VBM gives rise to the decrease of the hole's effective mass as the size of the tube increase from 4 to 12. However, for the tube (3, 3) in Fig. 6(a) compared to (4, 4), the curvature of the valence band increases largely as a result of state C and D crossover with
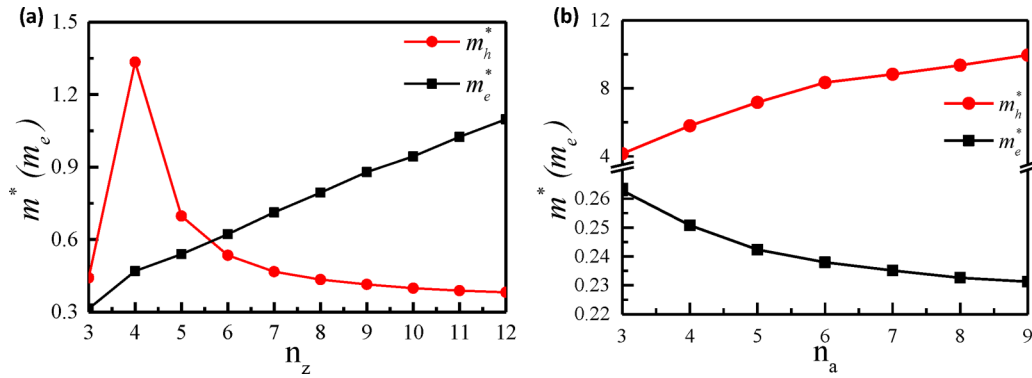
FIG. 11. The effective masses of the electron and hole for (a) z-TH-CNTs and (b) a-TH-CNTs as a function of tube size using the DFT calculations with PBE fucntionals.

state C being the VBM causing the sharp drop of the hole's effective mass.

On the other hand for the a-TH-CNT shown in Fig. 11(b), the effective mass of the hole increases from $4.16m_e$ to $9.96m_e$ with size ($13.88m_e$ in 2D tetrahex-C sheet) [19,21] due to the flattening of the valence band around the VBM caused by strain and charge distribution effect as shown in Figs. 6(e)–6(h). However, the effective mass of the electron stays close to that ($0.23m_e$ [19,21]) in 2D tetrahex-C sheet and decreases slightly from $0.26m_e$ to $0.23m_e$ with size (please note the scale difference before and after the break in the vertical axis). Correspondently, the curvature of the conduction band near the CBM exhibits no appreciable variation with the increasing tube size.

4. Work function

As a significant parameter for controlling field-emission properties, we calculated the work function of the TH-CNTs and the results are presented in Fig. 12. The work function refers to the energy difference between the Fermi (the middle of the gap) and vacuum levels, which is a common choice of defining work function in carbon nanotubes [38–40]. As
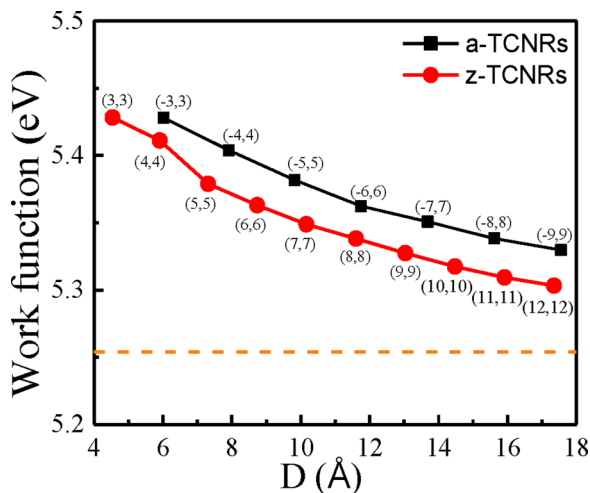

FIG. 12. The work functions in the TH CNTs as a function of tube size. The dashed line refers to the work function in the 2D tetrahex-C sheet.

mentioned above, the Fermi level for both tube cases reduces with the decreasing tube size. Thus the work function increases as the tube size decreases. It is found that the work function decreases from 5.43 to 5.30 eV with size for both a-TH-CNTs and z-TH-CNTs, approaching that of the tetrahex-C sheet (5.25 eV). Furthermore, a-TH-CNTs have slightly larger work functions than z-TH-CNTs given a similar size, which indicates that the electron in a-TH-CNTs is harder excite into vacuum than that in z-TH-CNTs.

IV. SUMMARY

We conducted first-principles DFT calculations to investigate the structural and electronic properties of the z-TH-CNTs and a-TH-CNTs with a tube diameter up to 18 Å. We found that the smallest thermodynamically stable nanotubes is (3, 3) for the z-TH-CNT with a diameter of 4.5 Å and (−3, 3) for the a-TH-CNT with a diameter of 6.0 Å, respectively. Since the 2D tetrahex-C nanosheet is in a buckled plane with a buckling thickness, the corresponding single-wall nanotubes have a particular wall thickness. It is found that the wall thickness of the tubes shrinks with smaller tubes. It is also found that the zigzag tubes are energetically more favorable than the armchair tubes given a similar size. It demonstrated that all studied nanotubes are semiconductors with a direct band gap at the center of the Brillion zone. The band gap is tunable in the range of 2.03–2.69 eV and 1.84–2.53 eV (located in the visible spectrum) from the HSE calculations for the z-TH-CNTs and a-TH-CNTs, respectively. It suggests that TH-CNTs can be utilized for optoelectronics, i.e., visible luminescing devices. The large curvature in small tubes alters their band structures largely. For the z-TH-CNTs, this effect results in a significantly reduced electron's effective mass thus potentially enhanced carrier mobility. The a-TH-CNTs with the whole observed range of tube size exhibit the small electron's effective mass suggesting potentially high carrier mobility. These remarkable structural and electronic properties in the tetrahex-C nanotubes may have potential applications in future nanoelectronics.

[1] K. S. Novoselov, A. K. Geim, S. V. Morozov, D. Jiang, Y. Zhang, S. V. Dubonos, I. V. Grigorieva, and A. A. Firsov, Science **306**, 666 (2004).

[2] K. S. Novoselov, A. K. Geim, S. V. Morozov, D. Jiang, M. I. Katsnelson, I. V. Grigorieva, S. V. Dubonos, and A. A. Firsov, Nature (London) **438**, 197 (2005).

[3] J. C. Meyer, A. K. Geim, M. I. Katsnelson, K. S. Novoselov, T. J. Booth, and S. Roth, Nature (London) **446**, 60 (2007).

[4] J. W. Mintmire, B. I. Dunlap, and C. T. White, Phys. Rev. Lett. **68**, 631 (1992).

[5] C. H. Kiang, M. S. Devries, G. Gorman, R. Savoy, D. S. Bethune, C. H. Klang, M. S. de-Vries, J. Vazquez, and R. Beyers, Nature (London) **363**, 605 (1993).

[6] N. Hamada, S. I. Sawada, and A. Oshiyama, Phys. Rev. Lett. **68**, 1579 (1992).

[7] R. Saito, M. Fujita, G. Dresselhaus, and M. S. Dresselhaus, Appl. Phys. Lett. **60**, 2204 (1992).

[8] S. Iijima, Nature (London) **354**, 56 (1991).

[9] S. Iijima and T. Ichihashi, Nature (London) **363**, 603 (1993).

[10] H. W. Kroto, J. R. Heath, S. C. O'Brien, R. F. Curl, and R. E. Smalley, Nature **318**, 162 (1985).

[11] L. C. Xu, R. Z. Wang, M. S. Miao, X. L. Wei, Y. P. Chen, H. Yan, W. M. Lau, L. M. Liu, and Y. M. Ma, Nanoscale **6**, 1113 (2014).

[12] Y. Liu, G. Wang, Q. Huang, L. Guo, and X. Chen, Phys. Rev. Lett. **108**, 225505 (2012).

[13] H. Lu and S. D. Li, J. Mater. Chem. C **1**, 3677 (2013).

[14] K. M. Merz, R. Hoffmann, and A. T. Balaban, J. Am. Chem. Soc. **109**, 6742 (1987).

[15] M. Zhao, W. Dong, and A. Wang, Sci. Rep. **3**, 3532 (2013).

[16] D. Malko, C. Neiss, F. Viñes, and A. Görling, Phys. Rev. Lett. **108**, 086804 (2012).

[17] S. Zhang, J. Zhou, Q. Wang, X. Chen, Y. Kawazoe, and P. Jena, Proc. Natl. Acad. Sci. USA **112**, 2372 (2015).

[18] A. J. Stone and D. J. Wales, Chem. Phys. Lett. **128**, 501 (1986).

[19] B. Ram and H. Mizuseki, Carbon N. Y. **137**, 266 (2018).

[20] Q. Wei, G. Yang, and X. Peng, Phys. Rev. Appl. **13**, 034065 (2020).

[21] X. Peng, Q. Wei, and G. Yang, Carbon N. Y. **165**, 37 (2020).

[22] Z. Wang, X. Cao, C. Qiao, R. J. Zhang, Y. X. Zheng, L. Y. Chen, S. Y. Wang, C. Z. Wang, K. M. Ho, Y. J. Fan, B. Y. Jin, and W. S. Su, Nanoscale **9**, 19310 (2017).

[23] W. Kohn and L. J. Sham, Phys. Rev. **140**, A1133 (1965).

[24] G. Kresse and J. Furthmuller, Phys. Rev. B **54**, 11169 (1996).

[25] G. Kresse and J. Furthmuller, Comput. Mater. Sci. **6**, 15 (1996).

[26] P. E. Blöchl, Phys. Rev. B **50**, 17953 (1994).

[27] G. Kresse and D. Joubert, Phys. Rev. B **59**, 1758 (1999).

[28] J. P. Perdew, K. Burke, and M. Ernzerhof, Phys. Rev. Lett. **77**, 3865 (1996).

[29] J. Heyd, G. E. Scuseria, and M. Ernzerhof, J. Chem. Phys. **118**, 8207 (2003).

[30] J. Heyd, G. E. Scuseria, and M. Ernzerhof, J. Chem. Phys. **124**, 219906 (2006).

[31] J. D. Pack and H. J. Monkhorst, Phys. Rev. B **16**, 1748 (1977).

[32] A. Togo and I. Tanaka, Scr. Mater. **108**, 1 (2015).

[33] G. G. Samsonidze, R. Saito, A. Jorio, M. A. Pimenta, A. G. Souza Filho, A. Grüneis, G. Dresselhaus, and M. S. Dresselhaus, J. Nanosci. Nanotechnol. **3**, 431 (2003).

[34] O. Dubay and G. Kresse, Phys. Rev. B **67**, 035401 (2003).

[35] R. A. Evarestov, A. V. Bandura, and V. V. Porsev, Lith. J. Phys. **56**, 164 (2016).

[36] X. Peng, Q. Wei, and A. Copple, Phys. Rev. B **90**, 085402 (2014).

[37] X. Peng and A. Copple, Phys. Rev. B **87**, 115308 (2013).

[38] B. Shan and K. Cho, Phys. Rev. Lett. **94**, 236602 (2005).

[39] B. Shan and K. Cho, Phys. Rev. B **73**, 081401(R) (2006).

[40] W. S. Su, T. C. Leung, and C. T. Chan, Phys. Rev. B **76**, 235413 (2007).